Author Manuscript

Author Manuscript

Author Manuscript

Author Manuscript

HHS Public Access

Author manuscript

Annu Int Conf IEEE Eng Med Biol Soc. Author manuscript; available in PMC 2022 September 18.

Published in final edited form as:

Annu Int Conf IEEE Eng Med Biol Soc. 2022 July ; 2022: 4397–4401. doi:10.1109/EMBC48229.2022.9871525.

Toward FBG-Sensorized Needle Shape Detection in Real Tissue Insertions

Min Jung Kim,

Department of Biomedical Engineering, Johns Hopkins University, Baltimore, MD 21218, USA

Dimitri A. Lezcano,

Department of Mechanical Engineering, Johns Hopkins University, Baltimore, MD 21218, USA

Jin Seob Kim [Member, IEEE],

Department of Mechanical Engineering, Johns Hopkins University, Baltimore, MD 21218, USA

Iulian I. Iordachita [Senior Member, IEEE]

Department of Mechanical Engineering, Johns Hopkins University, Baltimore, MD 21218, USA

Abstract

The determination of flexible needle shape during insertion is critical for planning and validation in minimally invasive surgical percutaneous procedures. In this paper, we validate a needle shape-sensing method using fiber Bragg grating (FBG) sensors over sequential needle insertion lengths in gel phantom and real tissue. Experiments on a four-active area, FBG-sensorized needle were performed in both isotropic simulated tissue and inhomogeneous animal tissue with computed tomography (CT) as the ground truth of the needle shape. The results show that the needle shape obtained from the FBG sensors has an overall consistent accuracy in real tissue in comparison to the phantom gel. The results validate a viable 3D needle shape-sensing model and reconstruction method over various insertion depths in comparison to the needle shapes determined from CT in both gel phantom and real tissue.

I. Introduction

Needle insertion is a common minimally invasive surgical procedure in procedures like prostate cryoablation and biopsy. However, tissue damage during needle insertion in tissue is common due to readjustments and reinsertions of the needle into the tissue — this is a well-known problem [1]. Furthermore, anatomical structures such as the bladder and certain vascular structures require complex insertion avoidance maneuvers [1]. The use of asymmetric bevel-tipped, flexible needles enables the surgeon to steer the needle; avoiding obstacles and reducing needle readjustments and reinsertions limits tissue damage to the patient. To place the needle at the prostate, an accurate understanding of the needle position during needle insertion is required.

Needle shape-sensing has been a commonly researched topic over the past few decades. Simple kinematic models like the unicycle and bicycle models founded developments of

mjkim@jhu.edu .

Author Manuscript Author Manuscript Author Manuscript Author Manuscript

needle shape-sensing and needle steering [2], [3]. Secoli developed the kinematic model for 3D shape estimation and closed-loop needle control by extending the bicycle model in 3D and the non-holonomic dynamics modeling of steerable needle insertions [3]. These models are well-defined and lightweight to implement but limit the needle shape's realization due to the constant curvature assumption founding the unicycle and bicycle models. Mechanics-based models based on classical beam theory have been used for determining needle shape, but they require detailed tissue information including tissue stiffness, viscoelasticity, and viscoelastic fracture to accurately model the needle shape [4]–[6]. Although these models allow for complex needle shape modelling, measurement of the model-dependent parameters may not be feasible pre-operatively or could change intra-operatively. A sensor-based, Lie-group theoretic model has been proven to provide accurate shape-sensing results allowing for complex 3D curvatures without depending on pre-operative tissue information using flexible needles embedded with fiber Bragg grating (FBG) sensors [7], [8]. The Lie-group theoretic model is founded on elastic rod theory and leverages Lie groups to enable 3D needle shape recognition based on FBG-based strain sensing.

In this paper, we evaluate our needle shape-sensing model in real inhomogeneous tissue over varying insertion depths using a four-active area needle under computed tomography (CT)-visualization. In Section II, we present our FBG sensor and 3D needle shape-sensing model used for our FBG-sensorized needle. Subsequently in Section III, we discuss our experimental setup and methods to perform needle insertion and shape-sensing under CT visualization. Finally, in Section IV, we discuss our experimental results and conclude the paper. The novelty of our work includes 3D shape reconstruction of a four-active area needle in real tissue over varying insertion depths coupled with our experimental setup and 3D shape confirmation method using CT imaging.

II. Methods

A. FBG Sensor Model

FBGs are Bragg reflectors inscribed in fiber optic cables with strain and temperature-sensing capabilities. As the cable is strained or undergoes a temperature change, the periodicity of the reflector changes and consequently changes the Bragg wavelength. The change in the peak Bragg wavelength with respect to the strain and temperature induced in the fiber optic cable can be approximated by:

$$\Delta\lambda = k_{\epsilon}\epsilon + k_T \Delta T \tag{1}$$

where ϵ is the strain induced in the FBG, ΔT is the temperature change in the FBG, and k_{ϵ} and k_T are the characteristic constants of the FBG associated with strain and temperature, respectively [9].

In our FBG-sensorized needle (Fig. 1), there are three FBG optical cables in a trigonal pattern array (120° relative to each other), each with four active sensing areas collocated along the length of the needle; the implemented sensors do not affect the invasiveness of the needle. To remove the effect of temperature in the FBGs, we first assume that k_T is constant for all the collocated FBGs (validated by temperature tests of these FBGs) and

Author Manuscript Author Manuscript Author Manuscript Author Manuscript

subtract the mean wavelength shift from each of the FBGs in each active area of the needle. This method enables direct strain measurements of the needle and is defined as *temperature compensation*.

For a Euler-Bernoulli rod, the curvature of the rod can be calculated as:

$$\kappa = \frac{\epsilon}{R} \tag{2}$$

where k is the curvature at a radius R in the rod. Using this information, we know that the change in the temperature-compensated Bragg wavelength is linearly proportional, $\overline{\Delta\lambda_i}$ (i = 1, 2, 3), to the curvature of the rod. Thus, a linear model for the cross-sectional curvature of the needle, $k_{xz,yz}$ (z-axis perpendicular to needle cross-section) can be determined along an FBG array by:

$$\omega = \left(\kappa_{xz}, \kappa_{yz}\right)^T = C(\Delta\lambda_1, \Delta\lambda_2, \Delta\lambda_3)^T \tag{3}$$

where $C \in \mathbb{R}^{2\times 3}$ is the calibration matrix, determined by the FBG-sensorized needle calibration process.

B. Lie-Group Theoretic Shape-Sensing Model

The sensor-based Lie-Group theoretic model [7] describes the curvature ((ω_1 and ω_2) along the local x- and y- axes, respectively) and torsion (ω_3 along the local z-axis) of the needle as:

$$\omega = (\omega_1, \omega_2, \omega_3)^T = \left(R^T(s)\frac{dR(s)}{ds}\right)^\vee \tag{4}$$

where $R(s) \in SO(3)$ is the orientation matrix in 3D space describing the local orientation of the body-fixed frame along the needle, $s \in [0, L]$ denotes the arclength of the needle, L is the length of the needle insertion, and $\vee$ operation defines a 3D vector with a 3 × 3 skew-symmetric matrix [10].

The needle is modelled as an inextensible elastic rod under uniformly distributed loads when inserting into homogeneous single-layered tissue. Due to the asymmetric bevel-tip of the needle, the needle will ideally deform in a single plane (yz-plane in the world frame), captured through introducing the intrinsic curvature of the needle $k_0(s)$. We can approximate the intrinsic curvature of the needle inserted into a single-layered homogeneous tissue using an intrinsic curvature constant, k_c, to combine the effect of the tissue's mechanical properties during needle insertion. Refer to [7] for a detailed explanation. Finally, the elastic potential energy of the rod is minimized by solving the Euler-Poincaré (E-P) equation [10], [11]. The intrinsic curvature constant and an initial deformation at the insertion base $\boldsymbol{\omega}_{init}$, obtained through optimization with the FBG sensor strain measurements, are used to determine the local angular deformation along the needle, $\boldsymbol{\omega}(s)$, which is in turn used to determine the 3D position of the needle, $\boldsymbol{r}(s)$, parameterized along the length of the needle.

Author Manuscript Author Manuscript Author Manuscript Author Manuscript

III. Experiment

A. Experimental Setup

The goal of this experiment is to determine whether the FBG-sensorized needle can provide accurate and real-time information during percutaneous procedures in real tissue and in gel phantoms. The experimental setup is presented in Fig. 2 and consists of Siemens ARCADIS Orbic 3D mobile C-Arm (Siemens Healthineers, Erlangen, Germany) to take the CT image, the gel phantom in an acrylic box, the FBG-sensorized needle encased in a 3D printed needle holder, and a laser-cut guide ensures consistent needle insertion depths with manual insertion.

Isotropic gel phantoms were constructed from normal plastic (M-F Manufacturing Company, TX, USA) to simulate tissue. Phantom gel tissue was created with liquid plastic without softener nor hardener. Smithfield Cooked Ham served as a realistic tissue model (Smithfield Foods, Smithfield, VA, USA), which was cut into the shape of the acrylic box (see Fig. 3a). Both tissues were designed to fit an acrylic box with dimensions allowing for 120 mm needle insertion depths. The acrylic box has seven 2 mm diameter steel balls as fiducials for image registration during analysis.

Tissue stiffness was measured with an OO durometer (ASTM 2240, MXBAOHENGus Instrument Co., China); the gel phantom had a stiffness of 38 units and the cooked ham had a stiffness of 50 units.

A 3D printed needle holder (see Fig. 3b and Fig. 3c) with six 3 mm diameter steel balls as fiducials ensures perpendicularity of the bevel tip to the tissue during manual insertion of the needle, and for image registration to determine the location of the needle relative to the tissue. A laser cut acrylic guide ensures needle insertion depth was incremented and consistent at the appropriate lengths of 30, 45, 60, 75, 90, 105, and 120 mm with manual insertion.

For this experiment, five full insertions were conducted with the bevel tip of the needle facing in each direction, for a total of ten insertions per tissue. Needle insertions were recorded for insertion depths of 30 mm and 105 mm for all insertions. For validation, the 3D needle shapes with FBG and CT modalities were collected for all seven insertion increments for two of the five insertions, for a total of four insertions per tissue.

B. CT Ground Truth Needle Shape

To determine the 3D ground truth needle shape when the needle is inserted into tissue, Siemens ARCADIS Orbic C-Arm was used to take a cone-beam CT image consisting of 256 × 256 × 256 voxels, representing 12 × 12 × 12 cm. The 3D needle shape is determined by binarizing the volume by isolating the voxels above a threshold of 1000 Hounsfield Units. The connected components in the binarized volume are then determined. The smallest seven fiducials are determined to be the 2 mm diameter fiducials embedded in the acrylic box and the largest connected component is determined to be the needle, which is then processed with cubic smoothing spline analysis at 0.5 mm increments along the length of the needle to interpolate needle position information. The FBG-based and CT-based needle shapes and

Author Manuscript Author Manuscript Author Manuscript Author Manuscript

their splines for two example trials at insertion depth of 105 mm for gel phantom tissue and cooked ham tissue, are shown in Fig. 4.

IV. Results

To compare the 3D needle shapes from the two modalities of FBG and CT, four types of 3D shape error metrics are considered: root means squared error (RMSE), in-bending-plane (*yz*-plane) error (IPE), out-of-bending-plane (*xz*-plane) error (OPE), and tip error (TE). RMSE is used to characterize overall shape correspondence, IPE is used to determine the error in the natural bending plane of the bevel-tipped needle, OPE is used to determine the errors associated with deflections out of the natural bending plane of the bevel tipped needle, and TE is used to determine the error distance between the bevel-tip of the two needle shapes. RMSE is defined between two 3D needle shapes $\{\mathbf{r}_1(s_i)\}_{i=1}^{N}$ and $\{\mathbf{r}_2(s_i)\}_{i=1}^{N}$ as:

$$RMSE = \sqrt{\frac{1}{N}\sum_{i=1}^{N}\left\|\mathbf{r}_1(s_i) - \mathbf{r}_2(s_i)\right\|^2} \tag{5}$$

where S_i is the parametrized arclength of each of the two needle shapes. The IPE is defined as:

$$IPE = \frac{1}{N}\sum_{i=1}^{N}\left\|(0\ \ 1\ \ 1)(\mathbf{r}_1(s_i) - \mathbf{r}_2(s_i))\right\|. \tag{6}$$

The OPE is defined as:

$$OPE = \frac{1}{N}\sum_{i=1}^{N}\left\|(1\ \ 0\ \ 1)(\mathbf{r}_1(s_i) - \mathbf{r}_2(s_i))\right\|. \tag{7}$$

The TE is defined as the Euclidean distance between the endpoints of the needle tips.

Using a paired-samples t-test, the p-values between gel phantom and cooked ham were 0.05, 0.65, 0.06, and 0.02 for RMSE, IPE, OPE, and TE, respectively. Taking a p-value of less than 0.05 to be statistically significant, only the TE was statistically significant between the two tissues, meaning that the detected location of the needle tip has a significantly greater error in real tissue, but otherwise there is no overall significant difference between the FBG-based needle shape in the gel and ham tissues.

When comparing the needle insertion depths of 30 mm, the p-values between gel phantom and cooked ham were 0.37, 0.27, 0.35, and 0.47 for RMSE, IPE, OPE, and TE, respectively. When comparing the needle insertion depths of 105 mm, the p-values between gel phantom and cooked ham were 0.07, 1.00, 0.13, and 0.03 for RMSE, IPE, OPE, and TE, respectively. As before, only the TE was statistically significant between the two tissues based on the p-value (less than 0.05). Thus, the detected location of the needle tip has a significantly greater error in real tissue, but otherwise there is no overall significant difference between the FBG-based needle shape-sensing capabilities in the gel and ham tissues. There is a larger variability in the TE for the cooked ham compared to the gel phantom (see Fig. 5) and for

Author Manuscript Author Manuscript Author Manuscript Author Manuscript

insertion depth of 105 mm compared to 30 mm in both gel and ham tissues (see Fig. 6). This result shows that the needle shape determined from the FBG has overall consistent accuracy in real tissue in comparison to the phantom gel.

Comparing the needle insertion depth of 30 mm to insertion depth of 105 mm in phantom gel, the p-values were 0.14, 0.44, 0.07, and 0.02 for RMSE, IPE, OPE, and TE, respectively. Again, using the same reasoning (i.e., p-value of less than 0.05 to be statistically significant), the TE difference was significant between the two insertion depths, which is consistently shown. In cooked ham, the p-values were 0.03, 0.14, 0.01, and 0.004 for RMSE, IPE, OPE, and TE, respectively. The RMSE, OPE, and TE differences were significant between the two insertion depths, with all error metrics having greater values at the insertion depth of 105 mm. This result shows that for greater insertion depths, the FBG-based needle shape may not be as accurate as shorter insertion depths during insertion into cooked ham; this advancement remains as future work.

Table I and Table II show the mean and standard deviation of the four 3D shape error metrics of each insertion depth for the four validation trials for the gel phantom and cooked ham tissues, respectively.

V. Conclusion

We presented 3D shape reconstruction of a four-active area needle under 3D CT visualization in real tissue over varying insertion depths coupled with our experimental setup and 3D shape confirmation method using CT. We determined that the FBG-sensorized needle can provide accurate and real-time information during percutaneous procedures in gel phantoms and in real tissue. In the future, the CT image and the needle shape determined from the FBG could be displayed in an imaging software such as 3D Slicer for planning and validation of the percutaneous procedure. Current limitations of this work include the manual insertion of the needle; this remains as a future work as we plan to run similar experiments using a robot to insert the needle. This improvement would allow higher accuracy in determining the needle position relative to the tissue. With these improvements, the real-time needle shape collected from the FBG during insertion could be used to navigate the bevel-tipped needle towards the target in clinical settings. We also plan to run similar experiments in more realistic tissue to simulate human tissue, such as heterogeneous raw animal meat and/or a realistic prostate gel phantom, such as the CIRS Model 053L (CIRS Inc., Norfolk, VA, USA).

Acknowledgments

This work has been supported by the National Institutes of Health under grant No. R01CA235134.

References

[1]. Matlaga BR, Eskew LA, and McCullough DL, “Prostate Biopsy: Indications and Technique,” J. Urol, vol. 169, no. 1, pp. 12–19, Jan. 2003, doi: 10.1016/S0022-5347(05)64024-4. [PubMed: 12478092]

Author Manuscript Author Manuscript Author Manuscript Author Manuscript

[2]. Webster RJ, Kim JS, Cowan NJ, Chirikjian GS, and Okamura AM, "Nonholonomic Modeling of Needle Steering," Int. J. Robot. Res, vol. 25, no. 5–6, pp. 509–525, May 2006, doi: 10.1177/0278364906065388.

[3]. Secoli R and Rodriguez y Baena F, "Closed-loop 3D motion modeling and control of a steerable needle for soft tissue surgery," in 2013 IEEE International Conference on Robotics and Automation, Karlsruhe, Germany, May 2013, pp. 5831–5836. doi: 10.1109/ICRA.2013.6631416.

[4]. Khadem M, Fallahi B, Rossa C, Sloboda RS, Usmani N, and Tavakoli M, "A mechanics-based model for simulation and control of flexible needle insertion in soft tissue," in 2015 IEEE International Conference on Robotics and Automation (ICRA), Seattle, WA, USA, May 2015, pp. 2264–2269. doi: 10.1109/ICRA.2015.7139499.

[5]. Khadem M, Rossa C, Sloboda RS, Usmani N, and Tavakoli M, "Mechanics of Tissue Cutting During Needle Insertion in Biological Tissue," IEEE Robot. Autom. Lett, vol. 1, no. 2, pp. 800–807, Jul. 2016, doi: 10.1109/LRA.2016.2528301.

[6]. Jiang S and Wang X, "Mechanics-Based Interactive Modeling for Medical Flexible Needle Insertion in Consideration of Nonlinear Factors," J. Comput. Nonlinear Dyn, vol. 11, no. 1, p. 011004, Jan. 2016, doi: 10.1115/1.4030747.

[7]. Kim JS, Chatrasingh M, Kim S, Suthakorn J, and Iordachita II, "Fiber Bragg Grating based needle shape sensing for needle steering system: Evaluation in inhomogeneous tissue," in 2017 IEEE SENSORS, Glasgow, Oct. 2017, pp. 1–3. doi: 10.1109/ICSENS.2017.8234074.

[8]. Chirikjian GS and Kyatkin AB, Harmonic Analysis for Engineers and Applied Scientists: Updated and Expanded Edition. Dover, 2016.

[9]. Park Wooram, Jin Seob Kim Yu Zhou, Cowan NJ, Okamura AM, and Chirikjian GS, "Diffusion-Based Motion Planning for a Nonholonomic Flexible Needle Model," in Proceedings of the 2005 IEEE International Conference on Robotics and Automation, Barcelona, Spain, 2005, pp. 4600–4605. doi: 10.1109/ROBOT.2005.1570829.

[10]. Holm DD, Marsden JE, and Ratiu TS, "The Euler–Poincaré Equations and Semidirect Products with Applications to Continuum Theories," Adv. Math, vol. 137, no. 1, pp. 1–81, Jul. 1998, doi: 10.1006/aima.1998.1721.

[11]. Kim JS and Chirikjian GS, "Conformational analysis of stiff chiral polymers with end-constraints," Mol. Simul, vol. 32, no. 14, pp. 1139–1154, Dec. 2006, doi: 10.1080/08927020601024137. [PubMed: 20198114]

Author Manuscript Author Manuscript Author Manuscript Author Manuscript

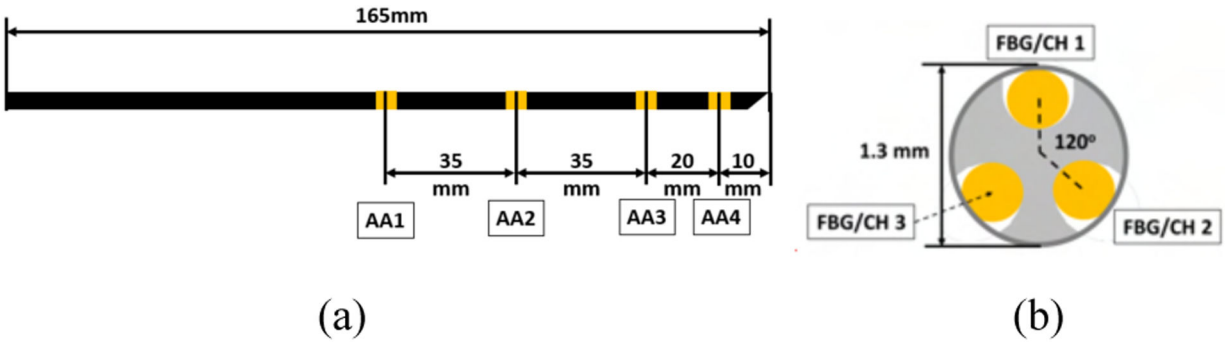

Figure 1.

The FBG-sensorized needle schematic. (a) Locations of the four active areas. (b) Orientation of the fiber optic cables in the needle.

Author Manuscript Author Manuscript Author Manuscript Author Manuscript

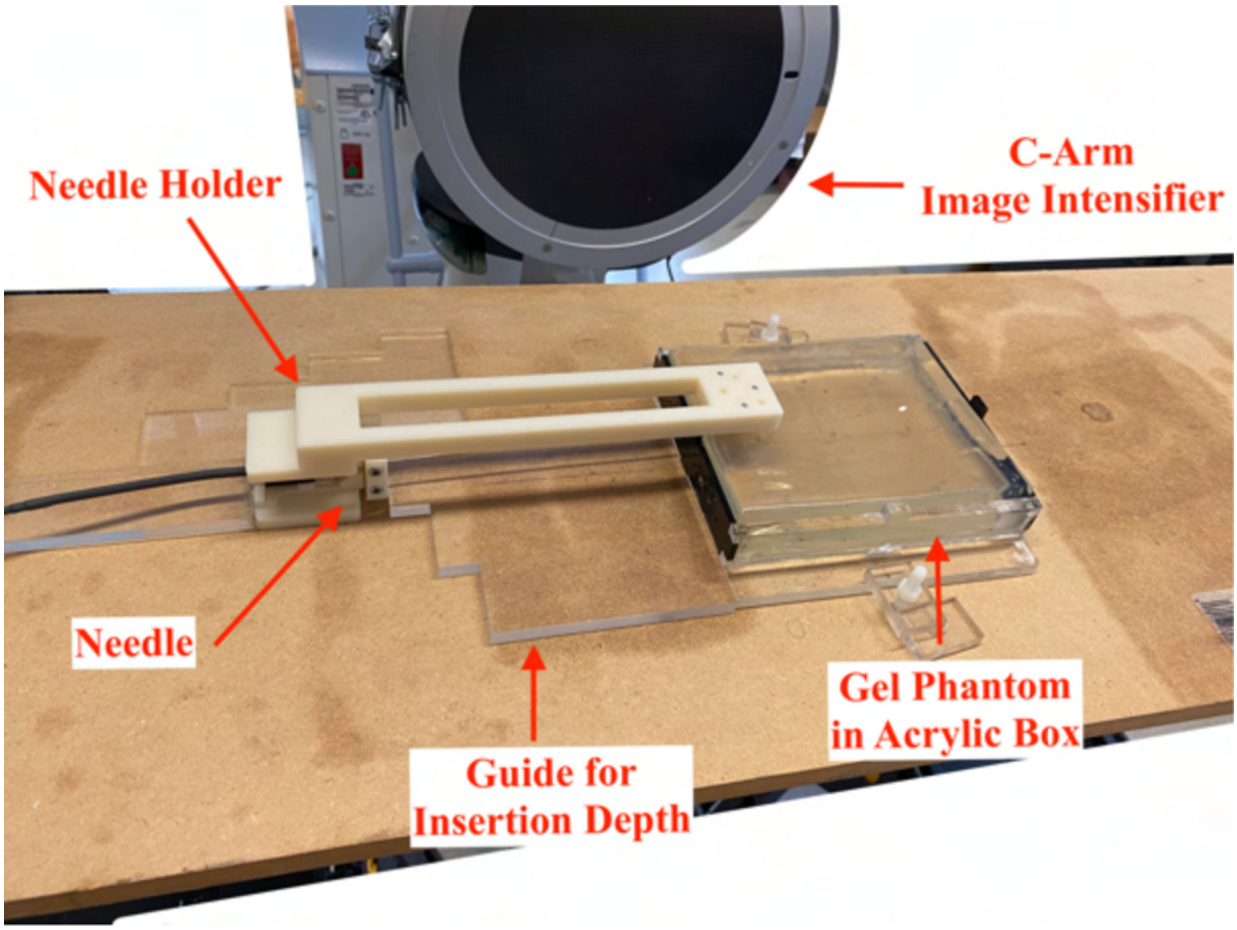

Figure 2.
Needle insertion experimental setup with gel phantom inside the C-Arm gantry.

Author Manuscript

Author Manuscript

Author Manuscript

Author Manuscript

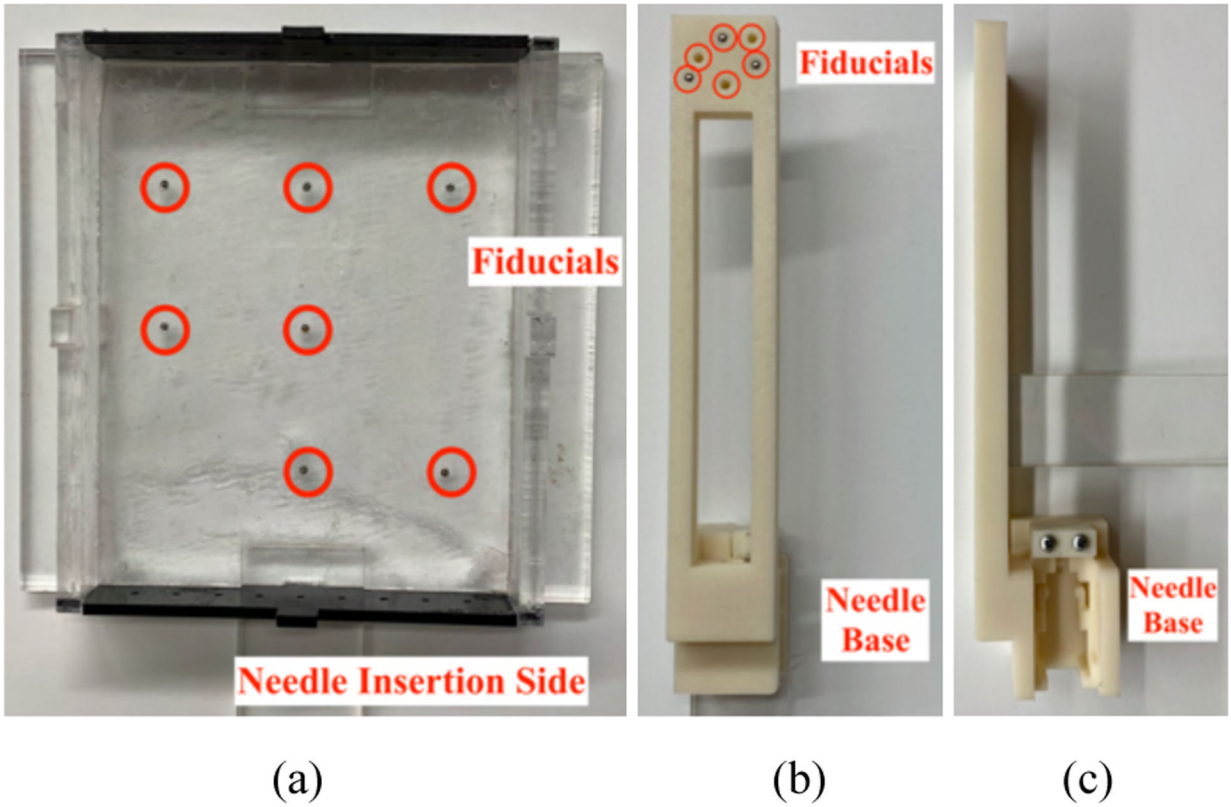

Figure 3.

(a) Top view of the acrylic box, with seven 2 mm diameter steel ball fiducials, circled in red. (b) Top view and (c) Side view of the 3D-printed needle holder, with six 3mm diameter steel ball fiducials, circled in red.

Author Manuscript Author Manuscript Author Manuscript Author Manuscript

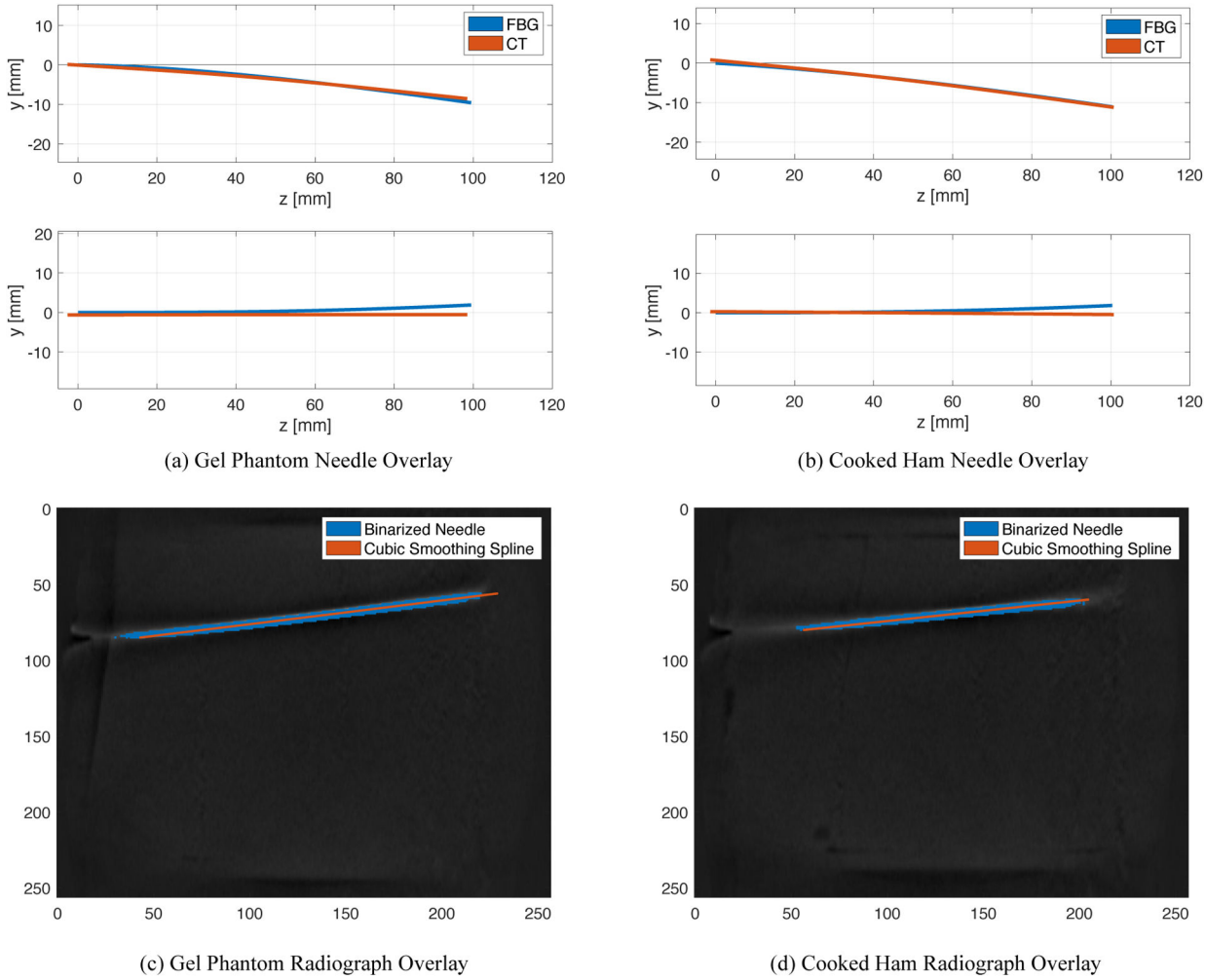

Figure 4.

Two example trials of FBG and CT needle shape-sensing in gel phantom and cooked ham at 105 mm needle insertion depth and the corresponding needle shape reprojections onto a single 2D radiographic slice from the obtained CT images.

Author Manuscript

Author Manuscript

Author Manuscript

Author Manuscript

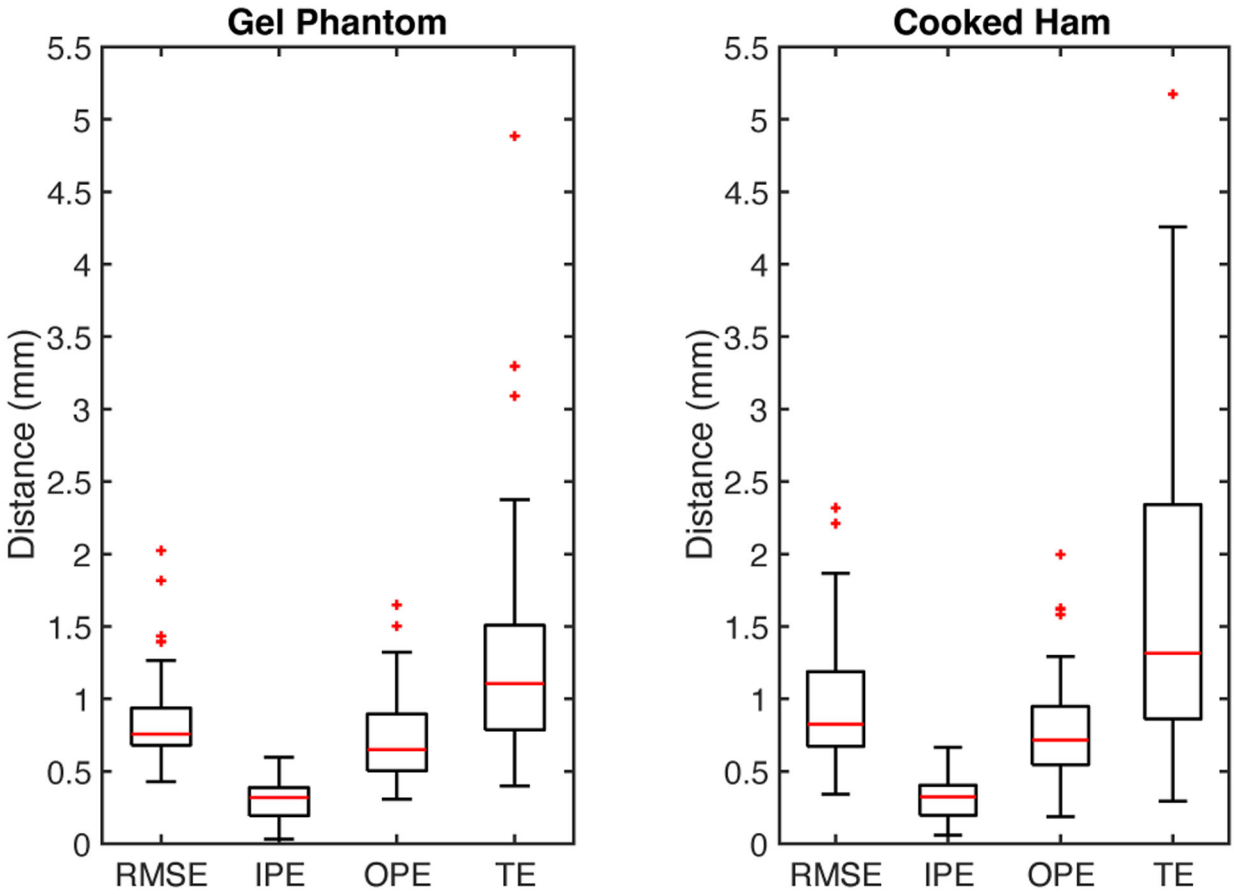

Figure 5.

3D Needle detection error metrics for gel phantom and cooked ham for all insertion depths.

Author Manuscript Author Manuscript Author Manuscript Author Manuscript

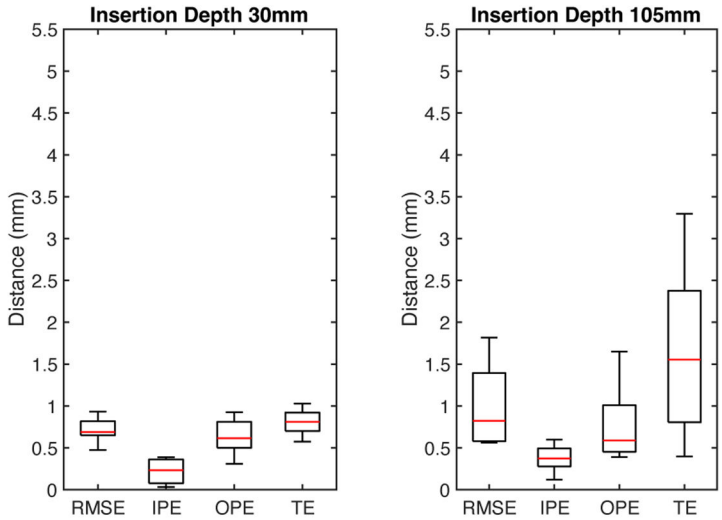

(a) Gel Phantom

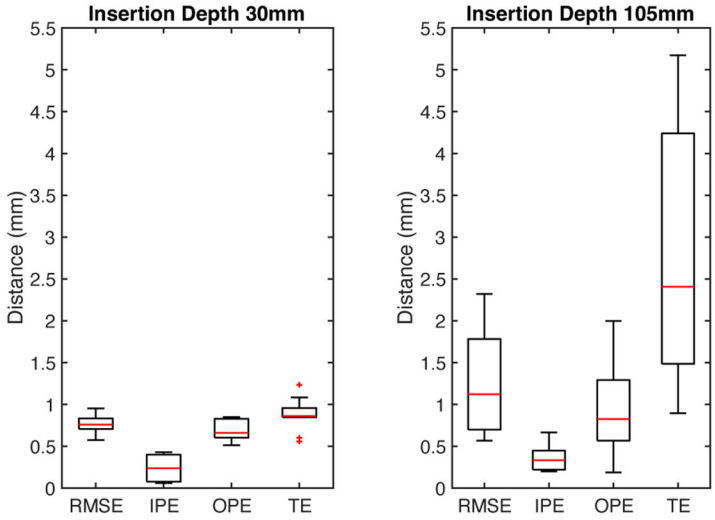

(b) Cooked Ham

Figure 6.

3D Needle detection error metrics for gel phantom and cooked ham at needle insertion depths of 30 mm and 105 mm.

Author Manuscript Author Manuscript Author Manuscript Author Manuscript

TABLE I.

Mean shape errors between the FBG-determined needle shape and the CT ground truth for gel phantom validation trials (mean ± standard deviation)

Insertion Depth (mm)	RMSE (mm)	IPE (mm)	OPE (mm)	TE (mm)
30	0.82 ± 0.11	0.19 ± 0.16	0.77 ± 0.15	0.97 ± 0.21
45	0.66 ± 0.17	0.22 ± 0.13	0.58 ± 0.15	0.99 ± 0.30
60	0.95 ± 0.24	0.29 ± 0.09	0.87 ± 0.22	1.25 ± 0.46
75	0.88 ± 0.38	0.31 ± 0.13	0.73 ± 0.39	1.14 ± 0.86
90	0.88 ± 0.22	0.34 ± 0.16	0.72 ± 0.20	1.46 ± 0.07
105	1.24 ± 0.47	0.51 ± 0.10	0.94 ± 0.52	2.29 ± 0.77
120	1.16 ± 0.60	0.41 ± 0.08	0.90 ± 0.46	2.05 ± 1.92

Author Manuscript

Author Manuscript

Author Manuscript

Author Manuscript

TABLE II.

Mean shape errors between the FBG-determined needle shape and the CT ground truth for cooked ham validation trials (mean ± standard deviation)

Insertion Depth (mm)	RMSE (mm)	IPE (mm)	OPE (mm)	TE (mm)
30	0.84 ± 0.14	0.21 ± 0.16	0.79 ± 0.16	1.05 ± 0.25
45	0.66 ± 0.42	0.23 ± 0.18	0.59 ± 0.38	0.95 ± 0.66
60	0.87 ± 0.36	0.29 ± 0.10	0.74 ± 0.34	1.05 ± 0.75
75	0.96 ± 0.59	0.28 ± 0.12	0.82 ± 0.52	1.74 ± 1.15
90	1.15 ± 0.52	0.34 ± 0.17	0.95 ± 0.47	2.34 ± 0.76
105	1.29 ± 0.69	0.43 ± 0.20	1.01 ± 0.66	2.59 ± 1.18
120	1.12 ± 0.27	0.38 ± 0.12	0.86 ± 0.18	2.17 ± 0.90